# Supporting Information

# Rational Construction of 3D Hierarchical Yolk-Shell $MnMoO_4$ Micro/Nanospheres for Electrochemical Energy Storage

*Yaxun Hu [a], Songtao Zhang [a]*, Xingyu Huang [a], Jinfeng Wang [a], Chenlu Zhao [a], Weifeng Peng [a], Xiaotian Guo [a], Guangxun Zhang [a], Yecan Pi [a], Tian Tian [a], Yi Xu [b]*, and Huan Pang [a,c]**

[a] School of Chemistry and Materials, Testing Center, Yangzhou University, Yangzhou, Jiangsu, 225009, P. R. China

[b] School of Physics and Materials Science, Nanchang University, Nanchang, Jiangxi, 330031, P. R. China

[c] School of Chemistry and Materials, Yangzhou Key Laboratory of Smart Materials and Clean Energy, Interdisciplinary Research Center for Advanced Energy, Yangzhou University, Yangzhou, 225002, Jiangsu, P. R. China.

*Corresponding author E-mail:

zhangsongtao@yzu.edu.cn (Songtao Zhang);

yixu@ncu.edu.cn (Yi Xu);

huanpangchem@hotmail.com, panghuan@yzu.edu.cn (Huan Pang)

## 1. Experimental section

### 1.1 Chemical reagent

All reagents were of analytical grade and could be used without further purification. Manganese nitrate tetrahydrate ($Mn(NO_3)_2$•$4H_2O$, 99%), molybdenum acetylacetone ($MoO_2(acac)_2$, 99%), and isopropanol ($C_3H_8O$, 99%) were purchased from Aladdin. Glycerol ($C_3H_8O_3$, 99%) was purchased from Sinopharm Chemical Reagent Co., LTD. Polyvinylidene fluoride was purchased from Meryer. All aqueous solutions were prepared with high-purity deionized water (DI water, resistance 18 MΩ•$cm^{-1}$).

### 1.2 Instrument required for experiment

The morphological features were characterized by field emission scanning electron microscopy (SEM, Zeiss-Supra55), transmission electron microscope (TEM, HT7800), and high resolution transmission electron microscopy (HRTEM, Tecnai G2 F30 S-TWIN). X-ray diffraction patterns (XRD) obtained from a Bruker D8 Advanced X-ray diffractometer equipped with Cu-Kα radiation (λ=0.15406 nm) using a 2θ range of 5−80$^o$ for characterization purposes. Raman spectroscopy was obtained by using Renishaw In Via Reflex (514 nm laser). X-ray photoelectron spectroscopy (XPS) analysis was performed using ESCALAB 250Xi X-ray photoelectron spectrometer. Raman spectra with a wavelength of 532 nm were acquired In Via a laser confocal Raman spectrometer (LabRAM HR Evolution, France). High resolution transmission electron microscopy (HRTEM) images, SAED images and energy dispersive X-ray spectra were captured on Tecnai G2 F30 transmission electron microscopy at 300 kV acceleration voltage. The specific surface area (SSA) was analyzed by Multipoint

Brunauer-Emmett-Teller (BET) technique. ICP-OES measurements were performed using a simultaneous ICP spectrometer (model Optima 7300 DV; PerkinElmer Inc., USA) equipped with a solid-state detector.

**1.3 Materials synthesis**

Synthesis of MnMoG glycerate spheres: The synthesis was based on the previously reported synthesis of MoG with some improvements.[1] Typically, $Mn(NO_3)_2 \cdot 6H_2O$ (0.25 mmol) and $MoO_2(acac)_2$ (0.25 mmol) were added into 40 ml of isopropanol (99%), and then 8 ml of glycerol (99%) were added, and stirred at 500 rpm for 30 min at room temperature, and then the obtained solution was transferred into a 100 ml Teflon-lined high-pressure reactor and maintained at 180 °C for 6 h. After being naturally cooled to room temperature, it was washed with ethanol. After natural cooling to room temperature, the precipitate was washed three times with ethanol and dried in an oven at 60 °C overnight. $Mn_xMo_yG$ with different metal ratios was prepared by adjusting the molar ratio of Mn and Mo.

Synthesis of yolk-shell $MnMoO_4$: 50 mg of prepared MnMoG glycerate solid spheres were weighed and placed in a porcelain boat and annealed in an air atmosphere heated at a ramp rate of 3 °C•$min^{-1}$ for 3 h at 500 °C to obtain the yolk-shell structure $MnMoO_4$. Only the annealing temperature was varied when the effect of calcination temperature was explored.

**1.4 Electrochemical measurements**

CHI 760e electrochemical workstation (CH Instrument, Shanghai Chenhua Instrument Cu, LTD, China) was used to conduct electrochemical performance experiments Cyclic

voltammetry (CV) and constant current charge-discharge (GCD) were used to test the samples at an electrochemical workstation.

For the three-electrode system, the working electrode was made by mixing the active materials, acetylene black, and polytetrafluoroethylene (PTFE) at a weight ratio of 80:15:5. Then, a few drops of isopropanol were added to the above mixture and coatedon nickel foam (1×1 $cm^{-2}$, current collector), which was next dried and pressed into a thin foil at a pressure of 8~10 MPa. The mass loading was 1.0~1.5 mg. The counter electrode and reference electrode were Pt wire and Hg/HgO (3.0 M KOH), respectively. The cyclic voltammetry (CV), and galvanostatic charge discharge (GCD) were tested on a CHI 760E electrochemical workstation in 3.0 M KOH. The specific capacitance (C) was calculated according to the following equations:

$$C = \frac{\int Idt}{m\Delta V}$$

$$C = \frac{Idt}{m\Delta V}$$

here, I represent discharge current (A), Δt represents discharge time (s), m represents mass of electroactive components (g) and ΔV represents potential window (V).

As for the asymmetrical supercapacitor, prepared materials and AC were used as positive electrode and negative electrode, respectively. The prepared materials (or AC), acetylene black, and PTFE were milled according to the above proportions and coated on nickel foam. The mass ratio of the electrode was determined by balancing the charges stored in each electrode. Generally, the charges stored by positive and negative electrodes can be calculated by $q_+ = C_+ \times \Delta E_+ \times m_+$ and $q_- = C_- \times \Delta E_- \times m_-$, where $C_+/C_-$

is the specific capacitance of positive/negative electrode ($F \bullet g^{-1}$); $\Delta E$ represents the potential range (V); $m_+/m_-$ is the weight of the active material in positive/negative electrode (g); The charges are balanced by the equation of $q_+ = q_-$, where $q_+/q_-$ represents the charges stored in the positive/negative electrode. Therefore, $m_+/m_- = C_- \times \Delta E_-/C_+ \times \Delta E_+$, the mass ratio between the negative and positive electrodes was set to 3:1 ~ 4:1. The typical mass loading of the active material in the positive electrode was 1.0~1.5 mg. The electrochemical tests of CV and GCD were also tested on a CHI 760E electrochemical workstation in 3.0 M KOH. The specific capacitance ($F\ g^{-1}$) was calculated according to the following equations:

$$C = \frac{\int Idt}{m\Delta V}$$

$$C = \frac{Idt}{m\Delta V}$$

here, I represent discharge current (A), $\Delta t$ represents discharge time (s), m represents mass of electroactive components (g) and $\Delta V$ represents potential window (V).

When assembling the asymmetric flexible all-solid-state device, the active material and AC were used as the positive and negative electrodes, respectively. A gel electrolyte consisting of 3 M KOH and polyacrylic acid (PAA) was employed. The assembled device was then encapsulated in a laminated plastic film. The mass ratio between the positive and negative electrodes was determined by balancing the charge stored in each electrode, following the charge-balance principle $m_+/m_- = C_- \times \Delta E_-/C_+ \times \Delta E_+$.

**Calculations of pseudocapacitive contribution:** The voltammetric response of an electrode at various sweep rates can be generally expressed as:

$$J = \alpha v^b$$

where, $j$ is the maxima of current densities (A $g^{-1}$), $\nu$ is the scan rate (mV•$s^{-1}$), $\alpha$ and $b$ are arbitrary coefficients. In general, when the b value approaches 1, capacitive process dominates. While the b value is about 0.5, the system is mainly controlled by diffusion process. Take the log of both sides of equation to obtain the slope as fitted parameter $b$:

$$\log j = \log \alpha + b \log \nu$$

where, $j_d$ is the current density at a particular voltage (A•$g^{-1}$), a and b are fitted parameters. The data were available when the fitting $R^2 > 0.97$. Contribution of pseudocapacitance at a given scanning rate:

$$j(V)/\nu^{1/2} = k_1 \nu^{\frac{1}{2}} + k_2$$

Where, ν is a specific voltage sweep speed, V is the specified voltage, $k_1$and $k_2$ are adjustable parameters. The $k_1$ is obtained by linear fitting of $j(V)/\nu^{1/2}$ and $\nu^{1/2}$ in formula. $k_1\nu$ at each particular voltage is the contribution of pseudocapacitance to the current.

## 2. SEM images of MnMo glycerate solid spheres with different molar ratios

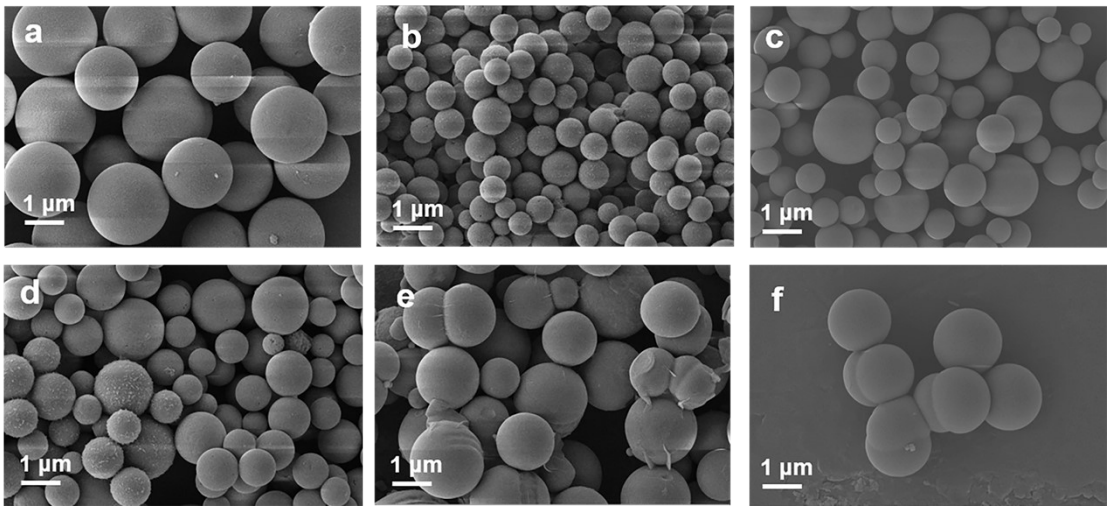


**Figure S1.** SEM images of (a) MnG, (b) $Mn_4MoG$ (Mn:Mo=4:1), (c) $Mn_2MoG$ (Mn:Mo=2:1), (d) $MnMo_2G$ (Mn:Mo=1:2), (e) $MnMo_4G$ (Mn:Mo=1:4), (f) MoG.

### 3. SEM, XRD and FT-IR patterns of materials with different solvent ratios

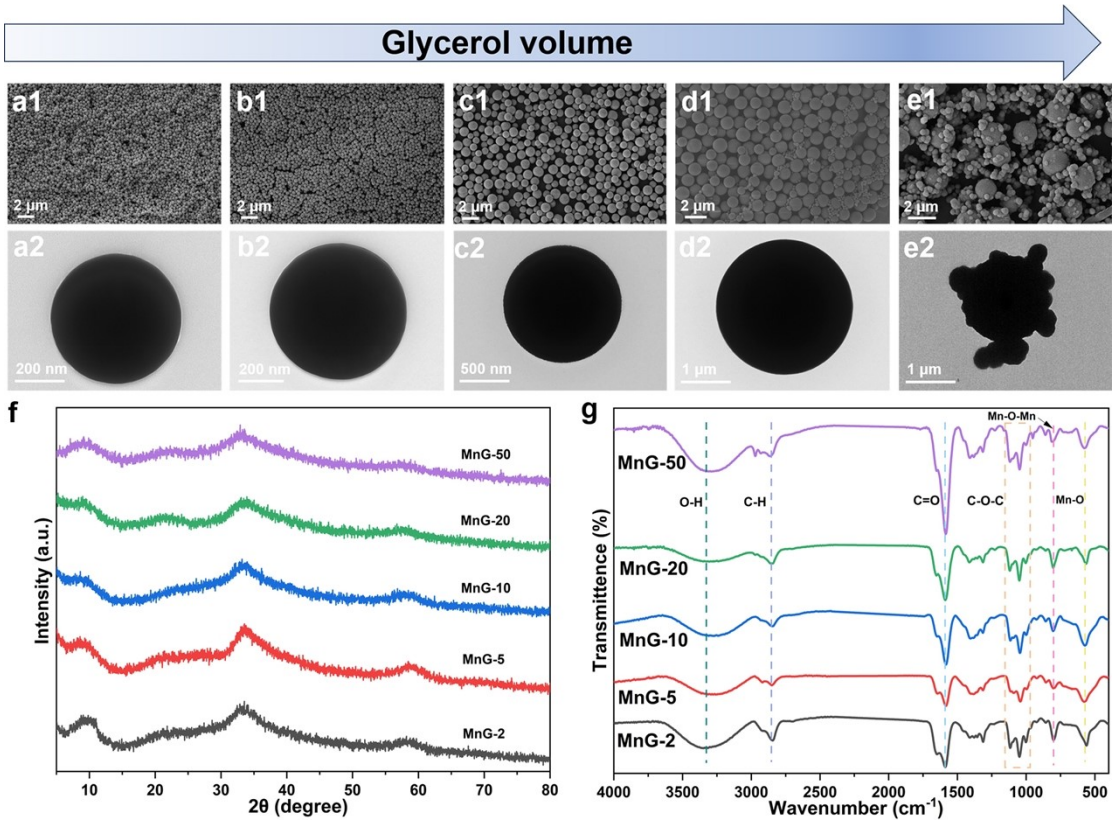


**Figure S2.** (a-e) SEM and TEM images, (f) XRD patterns, (g) FT-IR patterns of products with different solvent ratio.

## 4. SEM and XRD patterns of soak the materials for different times

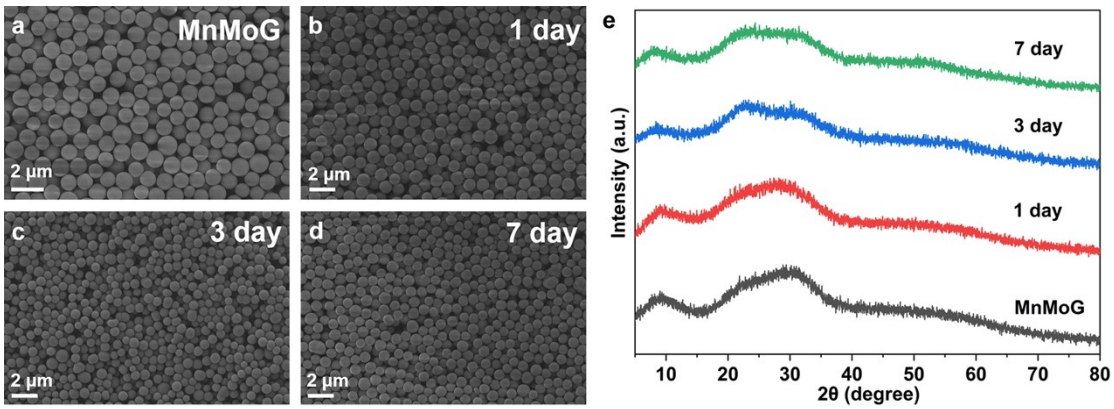


**Figure S3.** (a-d) SEM images, (e) XRD patterns of soak the materials for different times.

**5. Raman spectra of $Mn_xMo_y$ glycerate solid spheres with different molar ratios**

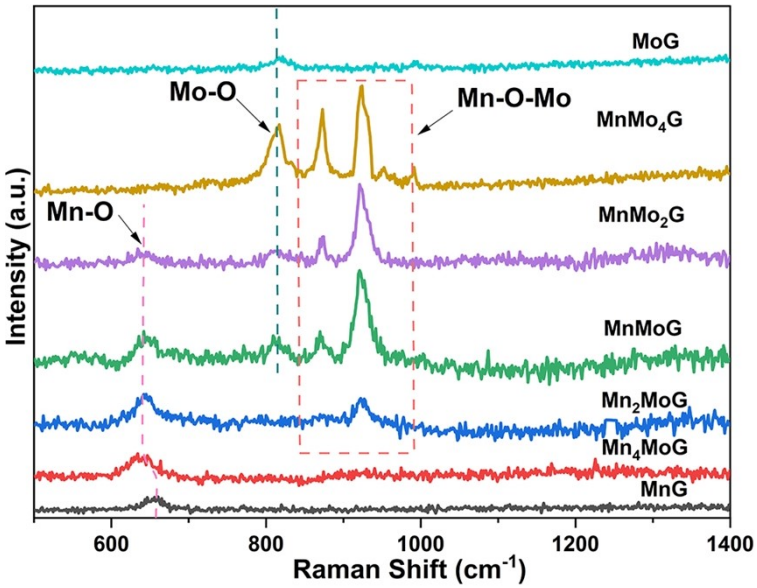


**Figure S4.** Raman spectra of $Mn_xMo_y$ glycerate solid spheres with different molar ratios.

## 6. Full XPS spectea of $Mn_xMo_yG$

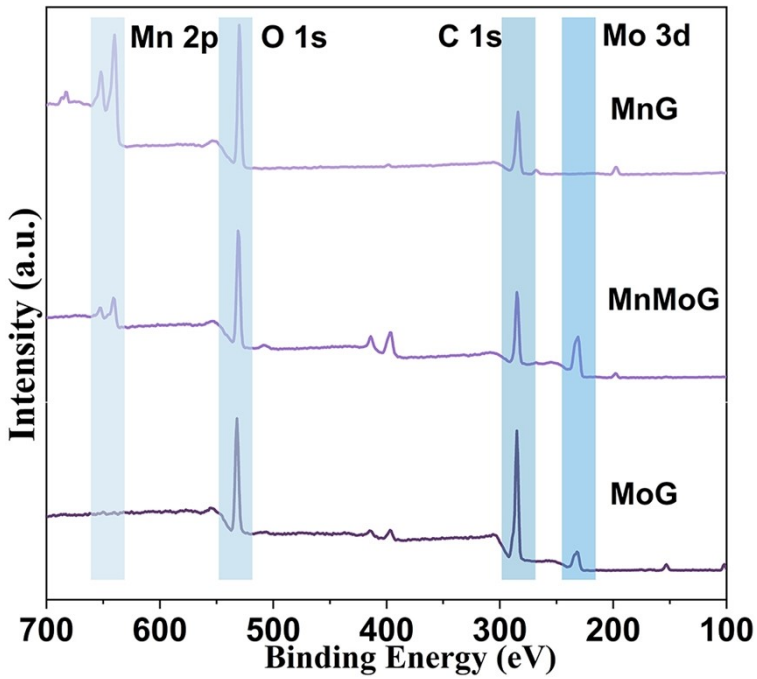


**Figure S5.** Full XPS spectea of $Mn_xMo_yG$.

**7. High-resolution XPS spectra of O 1s in the samples of in the samples of $Mn_xMo_yG$**

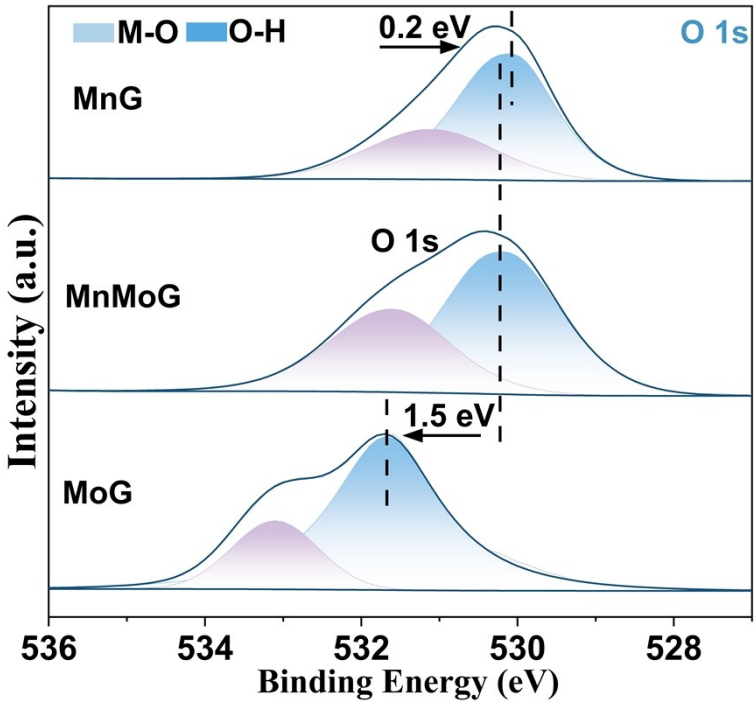


**Figure S6.** High-resolution XPS spectra of O 1s in the samples of in the samples of $Mn_xMo_yG$

**8. XRD spectra of materials with different calcination temperatures**

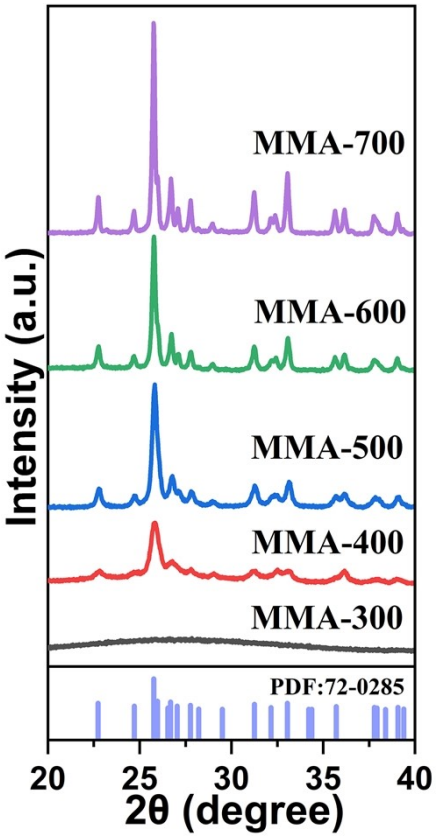


**Figure S7.** XRD spectra of materials with different calcination temperatures.

## 9. TEM images of MMA-500 at different calcination times

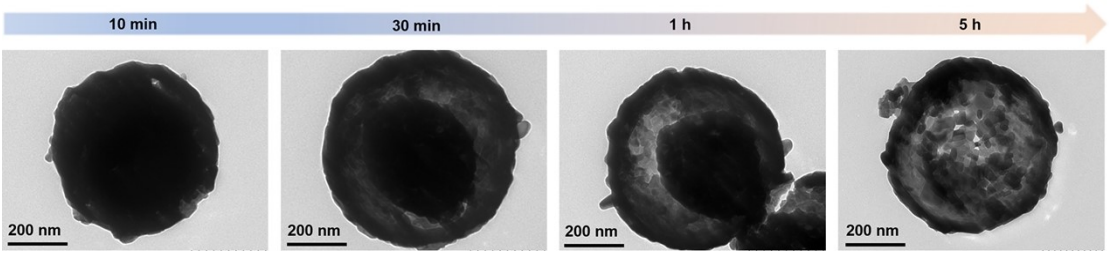


**Figure S8.** TEM images of MMA-500 at different calcination times.

## 10. EDX spectrum of $M_xM_yA$-500

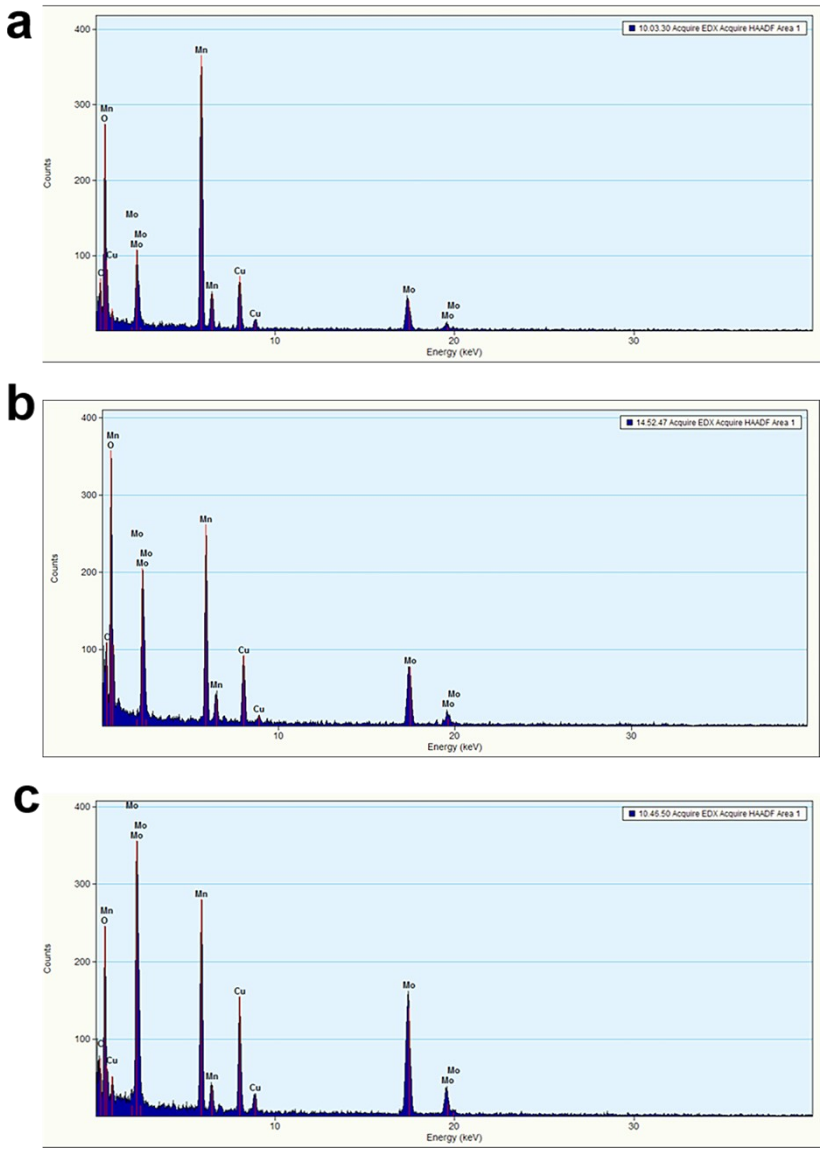


**Figure S9.** EDX spectrum of (a) $M_4MA$-500, (b) MMA-500, (c) $MM_4A$-500.

**11. Line scanning analysis of MMA-500**

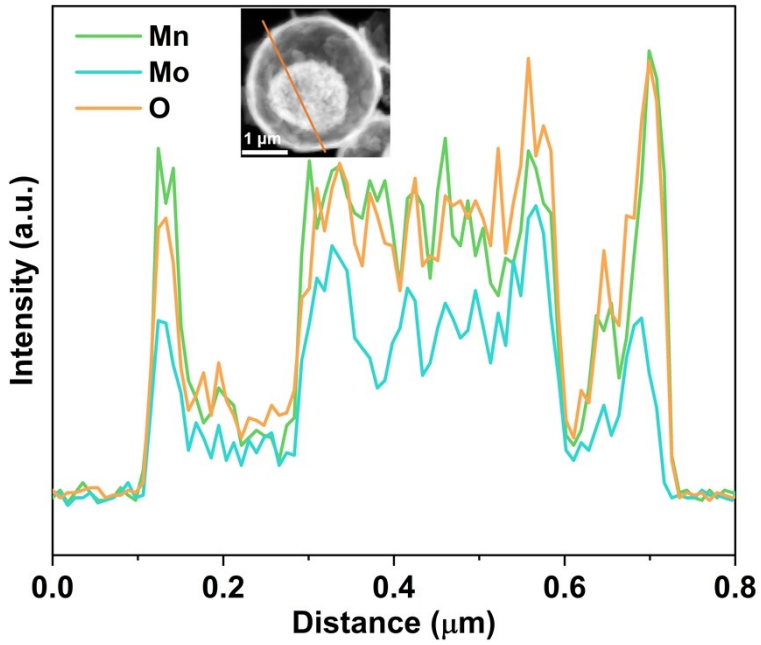


**Figure S10.** Line scanning analysis of MMA-500.

## 12. Powder photographs of $M_xM_yA$-500

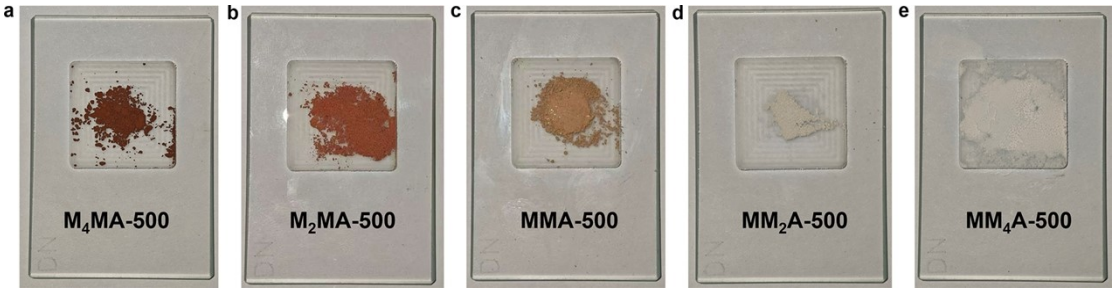


**Figure S11.** Powder photographs of $M_xM_yA$-500.

**13. Full XPS spectea of calcined products with different metal proportions**

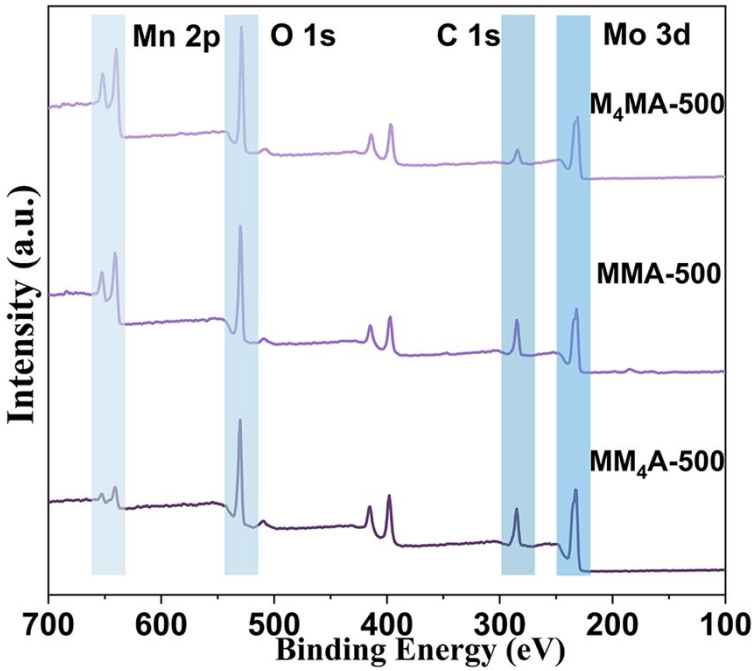


**Figure S12.** Full XPS spectea of calcined products with different metal proportions.

## 14. Electrochemical testing of calcination products with different metal ratios

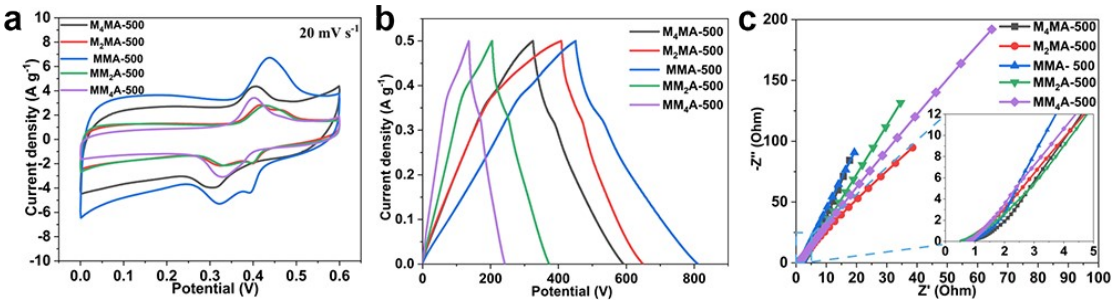


**Figure S13.** (a) CV curves at 20 mV•$s^{-1}$, (b) GCD curves at 0.5 A•$g^{-1}$, (c) EIS curves of calcination products with different metal ratios.

## 15. CV curves at different scan rates of electrode material

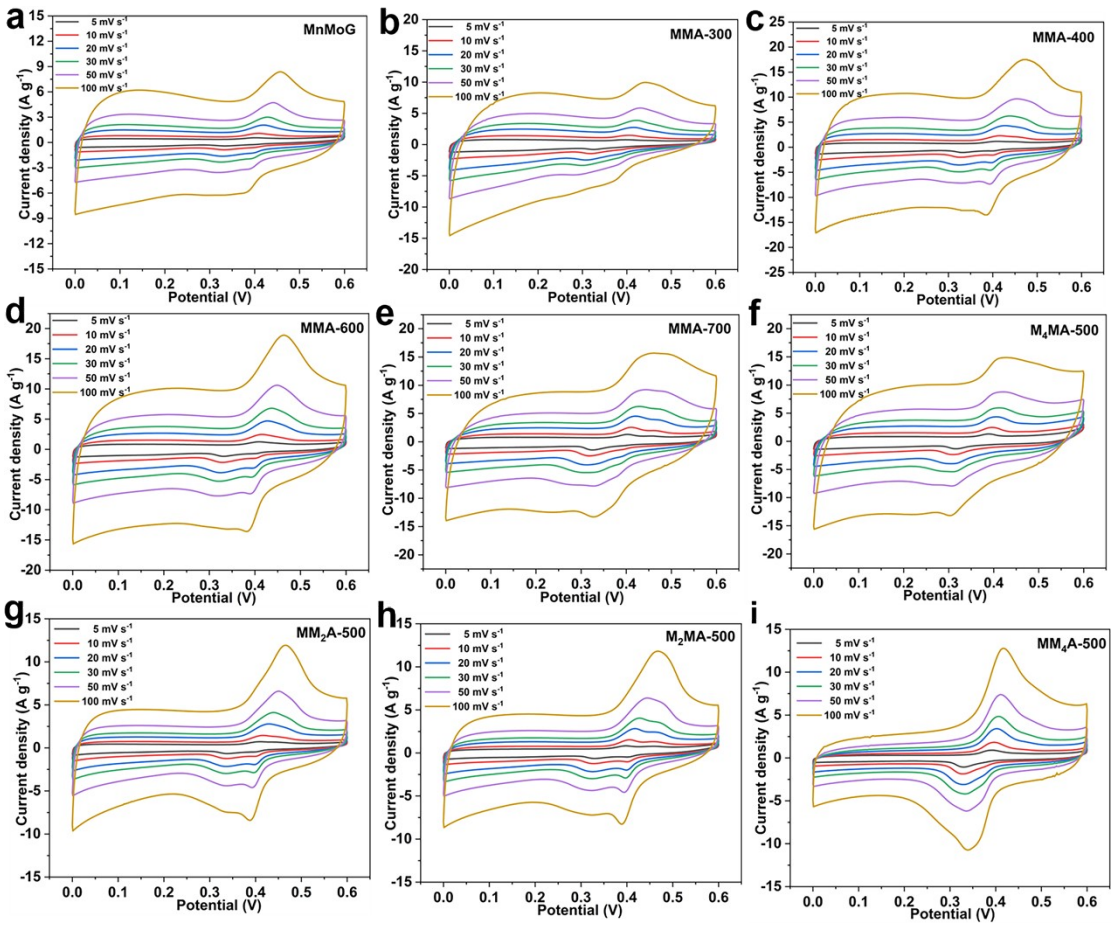


**Figure S14.** The CV curves at different scan rates of (a) MnMoG, (b) MMA-300, (c) MMA-400, (d) MMA-600, (e) MMA-700, (f) $M_4$MA-500, (g) $M_2$MA-500, (h) $MM_2$A-500, (i) $MM_4$A-500.

## 16. GCD curves at different scan rates of electrode material

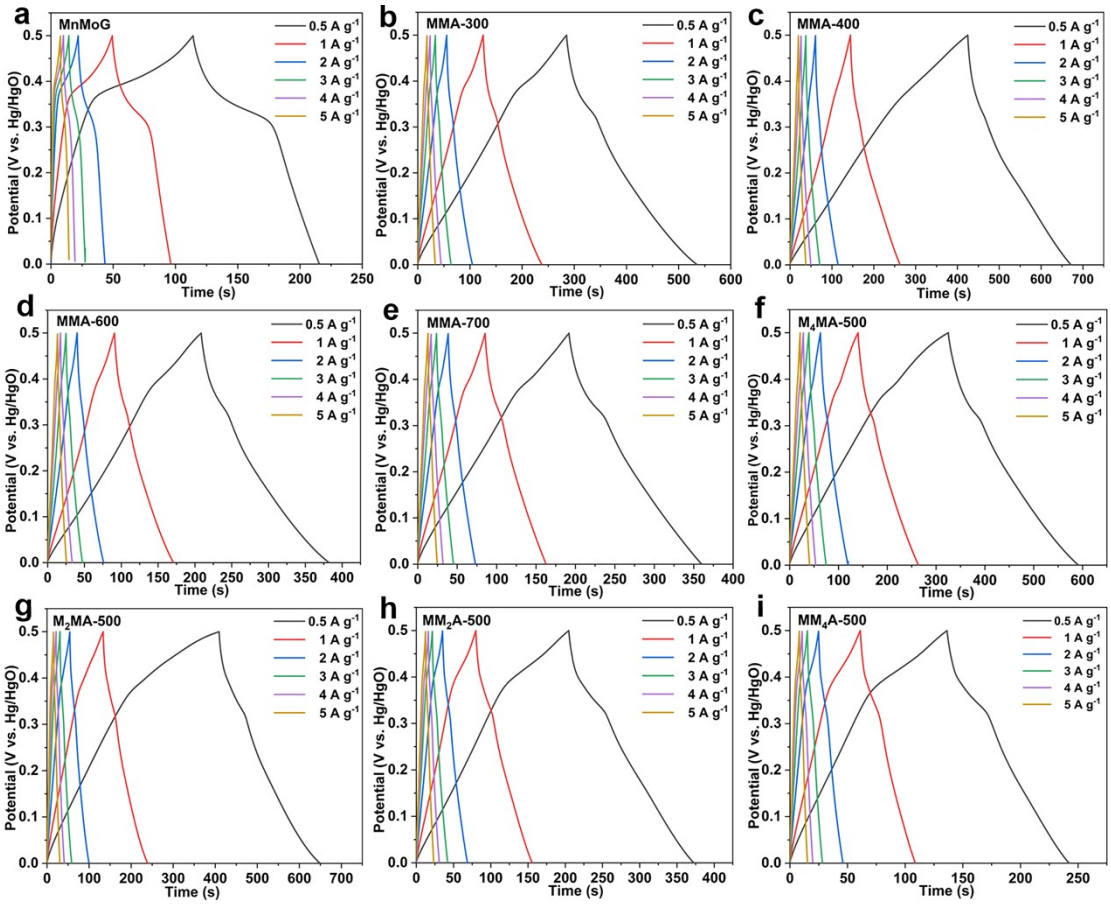


**Figure S15.** The GCD curves at different scan rates of (a) MnMoG, (b) MMA-300, (c) MMA-400, (d) MMA-600, (e) MMA-700, (f) $M_4$MA-500, (g) $M_2$MA-500, (h) $MM_2$A-500, (i) $MM_4$A-500.

.

**17. GCD curves at different scan rates of Ni foam**

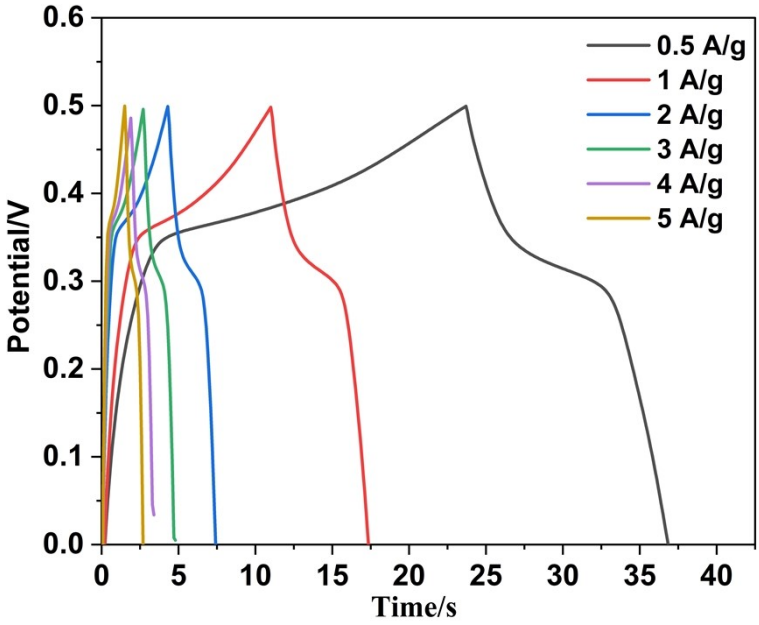


**Figure S16.** The GCD curves at different scan rates of Ni foam.

## 18. Capactitive contribution to total storage for the MMA-500

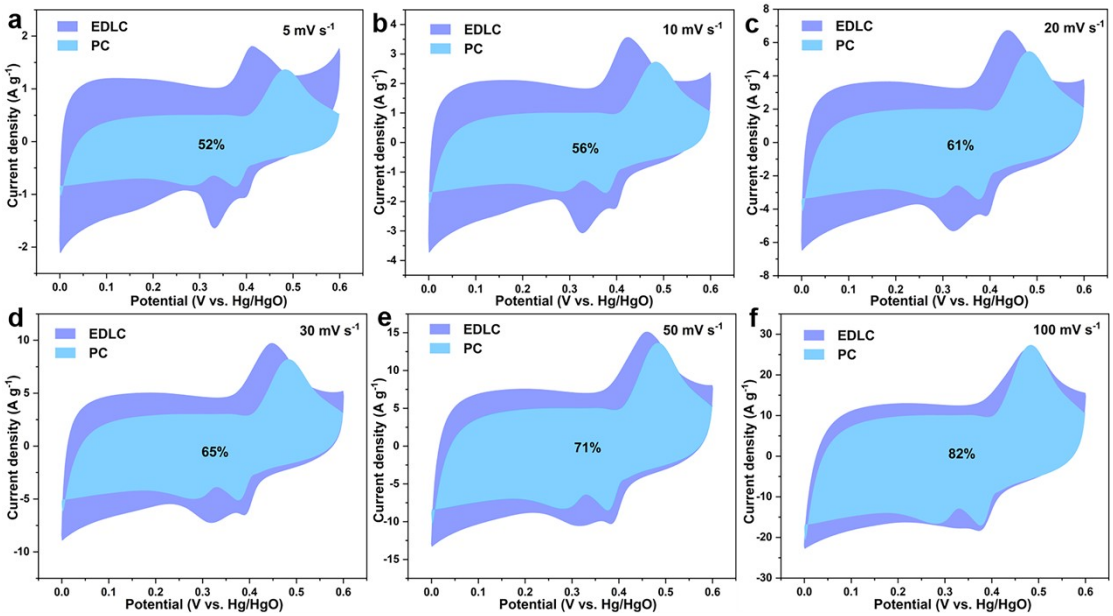


**Figure S17.** Total current (purple area) and capacitive-contributed current (blue area) of MMA-500 electrode at different scan rate.

## 19. b value of electrode material

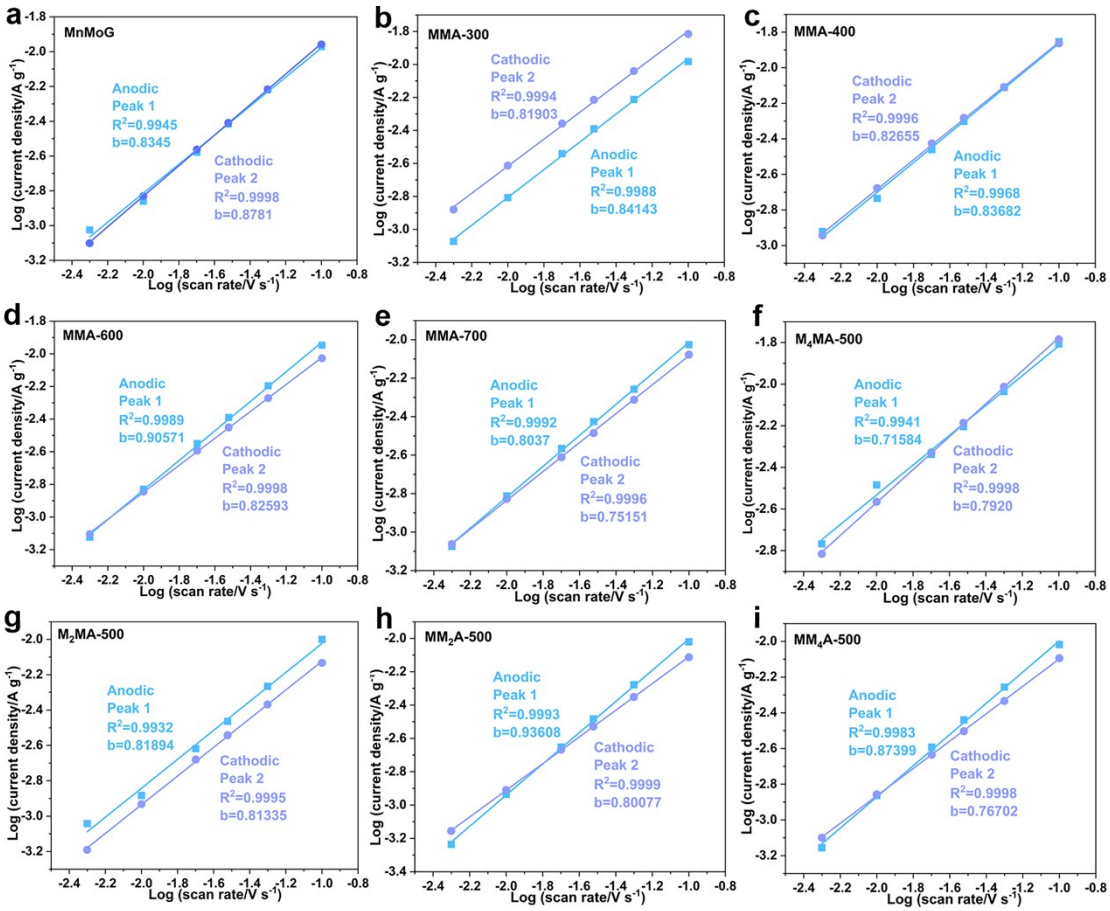


**Figure S18.** Corresponding *Log i* versus *log v* plots of the cathodic and anodic current response at the two pairs of peaks shown in CV curves of (a) MnMoG, (b) MMA-300, (c) MMA-400, (d) MMA-600, (e) MMA-700, (f) $M_4$MA-500, (g) $M_2$MA-500, (h) $MM_2$A-500, (i) $MM_4$A-500.

## 20. The percentages of capacitive contributions of electrode material

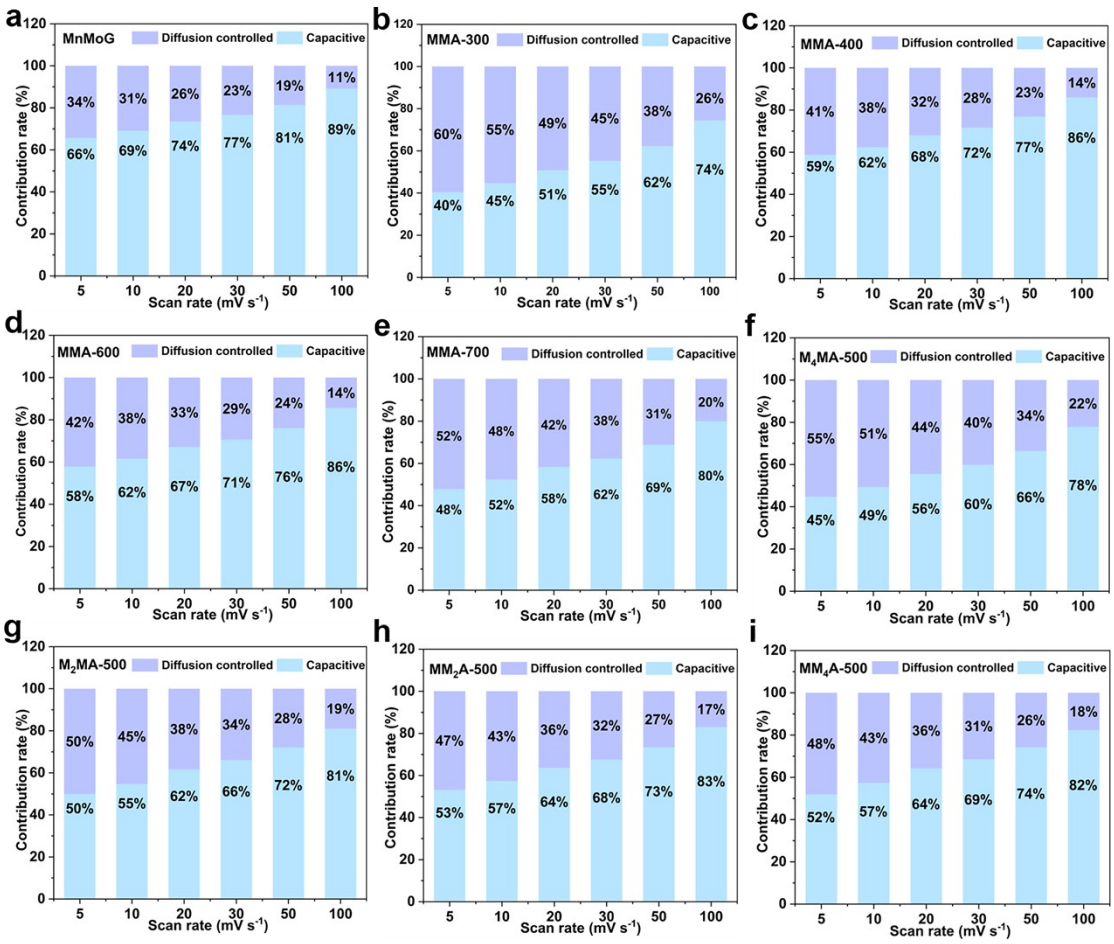


**Figure S19.** The percentages of capacitive contributions of (a) MnMoG, (b) MMA-300, (c) MMA-400, (d) MMA-600, (e) MMA-700, (f) $M_4$MA-500, (g) $M_2$MA-500, (h) $MM_2$A-500, (i) $MM_4$A-500.

**21. CV curves of MMA-500//AC under different potential Windows**

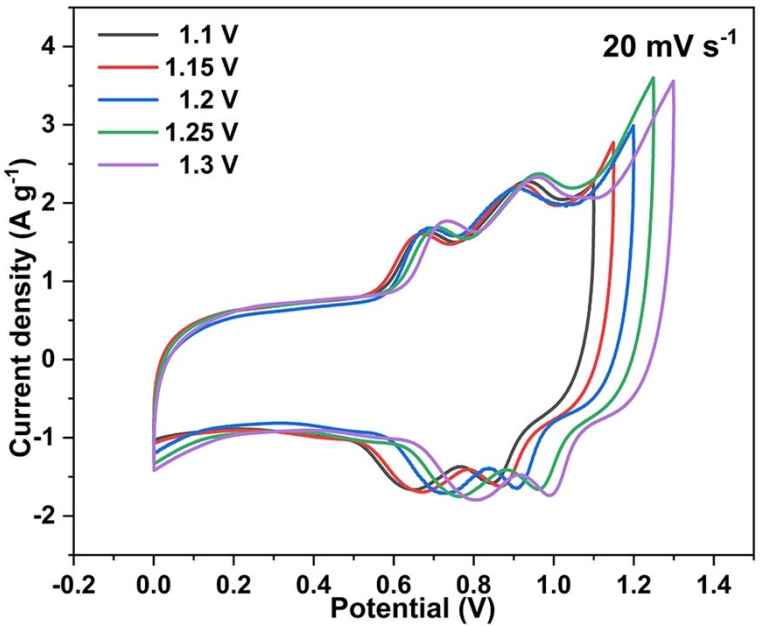


**Figure S20.** CV curves under different potential Windows.

**22. CV curves of the first three cycles of MMA-500//AC**

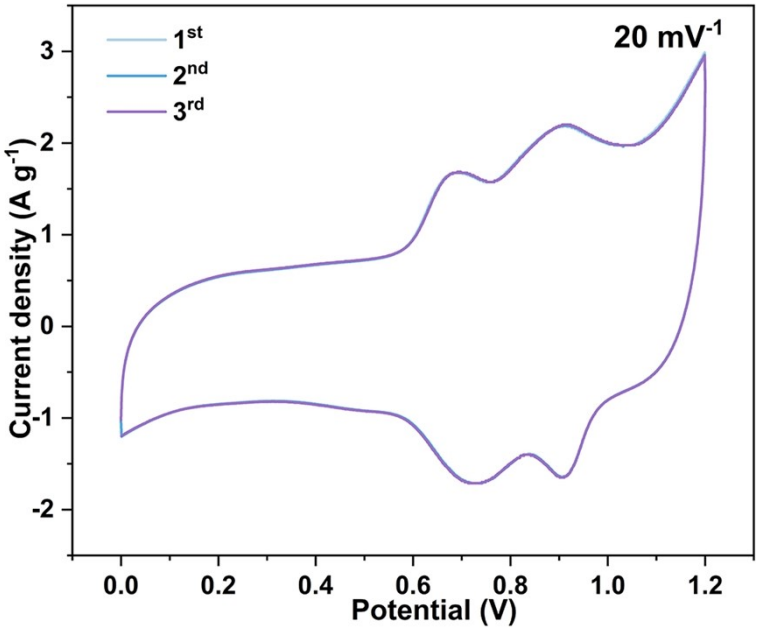


**Figure S21.** CV curves at a scan of 20 mV•$s^{-1}$ of the initial three cycles.

## 23. Capactitive contribution to total storage for the MMA-500//AC

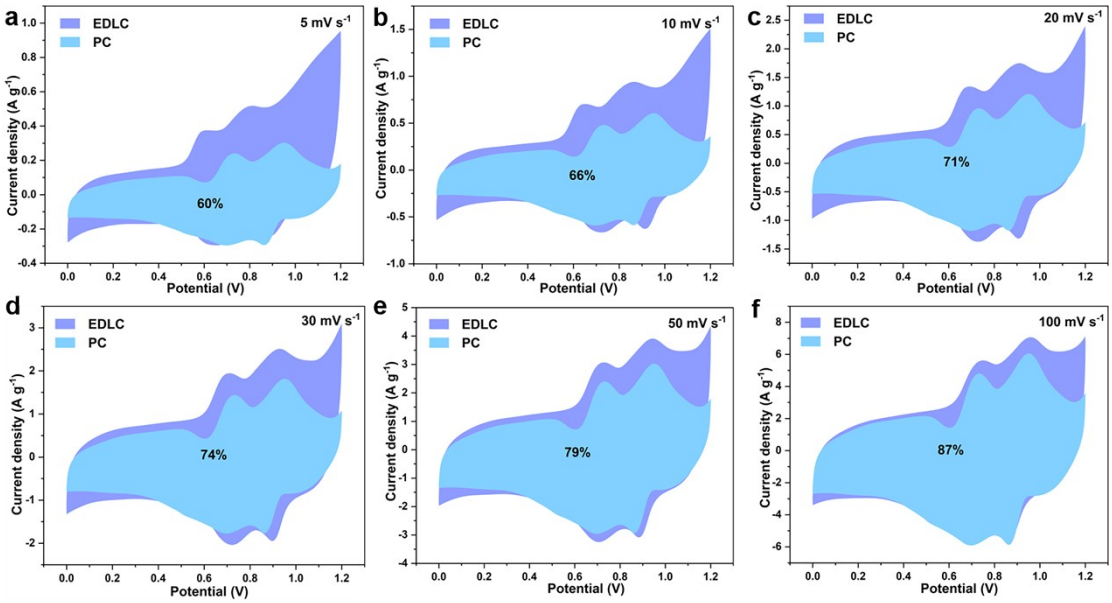


**Figure S22.** Total current (purple area) and capacitive-contributed current (blue area) of MMA-500//AC electrode at different scan rate.

**24. XRD spectra of electrode material after long cycling**

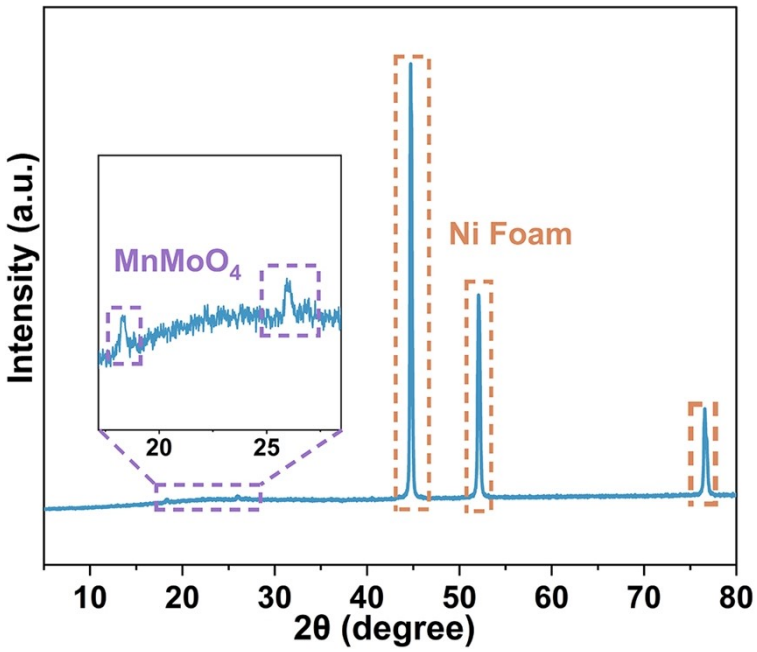


**Figure S23.** XRD spectra of electrode material after long cycling.

**25. SEM images of electrode material after long cycling**

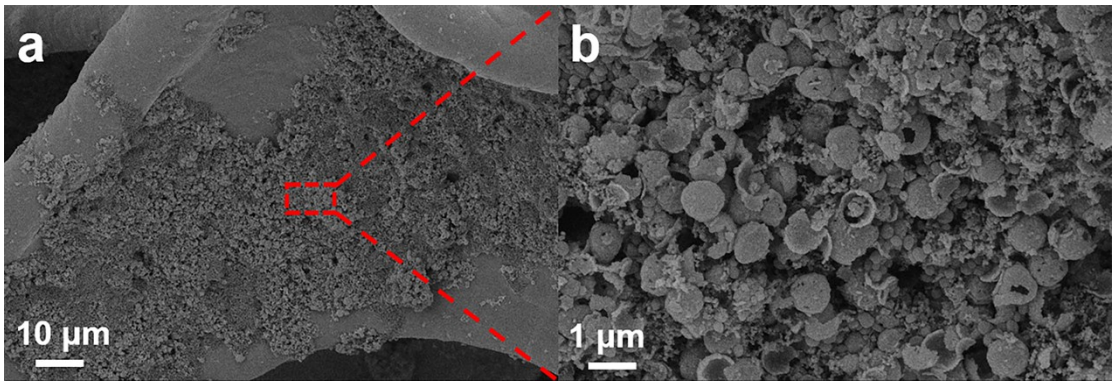


**Figure S24.** SEM images of electrode material after long cycling.

**Supplementary Tables:**

**Tables S1.** Comparison of the main synthesis methods of yolk-shell materials.

| Yolk-shell materials | Synthesis method | Synthesis condition | Ref |
|---|---|---|---|
| $TiO_2@SiO_2$ | Selective etching | 10% HF, 30 ℃, 10 min | 2 |
| Fe-$Co_xP$ | | $NaH_2PO_2$, 3 ℃/min, 350 ℃, 2h | 3 |
| $Au@Cu_2O$ | Ostwald ripening | 0.2 M NaOH, 15 min of stirring | 4 |
| Ag@Cu | | DMF, 160 ℃, 11h | 5 |
| Cu@Ru HHNS | Kirkendall diffusion | H2, 1.5 ℃/min, 300 ℃, 1h | 6 |
| $Cu@Au_3Cu@CdS$ | | 10 mL toluene, 50 μL TBP, oil bath at 45℃ for 30 min | 7 |
| $NiCo_2O_4$ | Self-templating approach | Air, 1 ℃/min, 350 ℃, 2h | 8 |
| CoOOH | | 0.75 mL water, 0.25 mL IPA, and 50 mL of 5% Nafion solution, sonication for 30 min | 9 |
| Y-$CoMoO_4$ | | Air, 1 ℃/min, 550 ℃, 2h | 10 |
| **$MnMoO_4$** | | **Air, 3 ℃/min, 500 ℃, 3h** | **This work** |

**Tables S2.** ICP−OES Analyses of $Mn_xMo_yG$.

| Samples | Mn detected (Molar ratio) | Mo detected (Molar ratio) |
|---|---|---|
| MnG | 1 | - |
| $Mn_4MoG$ | 0.78 | 0.22 |
| $Mn_2MoG$ | 0.66 | 0.34 |
| MnMoG | 0.55 | 0.45 |
| $MnMo_2G$ | 0.39 | 0.61 |
| $MnMo_4G$ | 0.24 | 0.76 |
| MoG | - | 1 |

**Table S3.** The physical properties of as-prepared material**.**

| Samples | $S_{BET}$ ($m^2 \cdot g^{-1}$) | Pore volume ($cm^3 \cdot g^{-1}$) | Average pore size (nm) |
|---|---|---|---|
| MnMoG | 25.98 | 0.053 | 8.23 |
| MMA-300 | 54.12 | 0.251 | 5.584 |
| MMA-400 | 109.49 | 0.179 | 5.167 |
| MMA-500 | 171.31 | 0.281 | 5.878 |
| MMA-600 | 193.84 | 0.263 | 6.642 |
| MMA-700 | 37.66 | 0.083 | 8.774 |

**Table S4.** The elemental molar ratio of $M_xM_yA$-500 was derived from the XPS report.

| Element | Mn (%) | Mo (%) | Mn:Mo molar |
|---|---|---|---|
| $M_4MA$-500 | 11.98 | 3.21 | 3.73:1 |
| MMA-500 | 7.13 | 6.34 | 1.12:1 |
| $MM_4A$-500 | 1.17 | 4.85 | 1:4.14 |

**Table S5.** Electrochemical performance characterization of $MnMoO_4$ by using a three-electrode test system in recent years.

| Materials | Electrolytes | Specific capacitance | Cycling stability | Ref |
|---|---|---|---|---|
| MnAC ($Mn_3O_4$) | 3 M KOH | 120 F $g^{-1}$ (0.5 A $g^{-1}$) | 94% (0.5 A $g^{-1}$, 1000) | 11 |
| $MnO_2$/$Mn_2O_3$ | 1 M KOH | 182 F $g^{-1}$ (0.5 A $g^{-1}$) | 90.1% (5 A $g^{-1}$, 5000) | 12 |
| $Mn_3O_4$ | 6 M KOH | 273.3 F $g^{-1}$ (0.5 A $g^{-1}$) | 82 % (5 A $g^{-1}$, 10000) | 13 |
| RGO/$SnO_2$/ $Mn_3O_4$-$Mn_2O_3$ | 3 M KOH | 312 F $g^{-1}$ (0.5 A $g^{-1}$) | 97.28% (10 A $g^{-1}$, 5000) | 14 |
| $MoO_3$ | 1 M KOH | 244.35 F $g^{-1}$ (0.5 A $g^{-1}$) | 109.2% (2 A $g^{-1}$, 5000) | 15 |
| $MoO_3$ nanosheets | 3 M KOH | 256 F $g^{-1}$ (0.5 A $g^{-1}$) | - | 16 |
| Pd/$MoO_3$–rGO | 6 M KOH | 291.5 F $g^{-1}$ (0.5 A $g^{-1}$) | 88.46% (1 A $g^{-1}$, 1000) | 17 |
| $MnMoO_4$ | 3 M KOH | 120.12 F $g^{-1}$ (0.5 A $g^{-1}$) | 95 % (0.5A $g^{-1}$, 10000) | 18 |
| $MnMoO_4$@1T-$MoS_2$ | 6 M KOH | 319 F $g^{-1}$(1 A $g^{-1}$) | 83.2% (10 A $g^{-1}$, 10000) | 19 |
| $MnMoO_4$ | 3M KOH | 325.5 F $g^{-1}$ (1 A $g^{-1}$) | 78.1% (1 A $g^{-1}$, 120 min) | 20 |
| $MnMoO_4$ Nanorods | 3M KOH | 13.1 F $g^{-1}$ (1 A $g^{-1}$) | - | 21 |
| **MMA-500 (Yolk-shell $MnMoO_4$)** | **3 M KOH** | **361.4 F $g^{-1}$ (0.5 A $g^{-1}$)** | **81.14% (5A $g^{-1}$, 9000)** | **This work** |

## References


1 Y. Wang, L. Yu and X. W. (David) Lou, Formation of Triple-Shelled Molybdenum-Polydopamine Hollow Spheres and Their Conversion into MoO2/Carbon Composite Hollow Spheres for Lithium-Ion Batteries, *Angew. Chem. Int. Ed.*, 2016, **55**, 14668–14672.

2 D. Chen, L. Li, F. Tang and S. Qi, Facile and scalable synthesis of tailored silica "nanorattle" structures, *Adv. Mater.*, 2009, **21**, 3804–3807.

3 W. Song, X. Teng, Y. Niu, S. Gong, X. He and Z. Chen, Self-templating construction of hollow Fe-CoxP nanospheres for oxygen evolution reaction, *Chem. Eng. J.*, 2021, **409**, 128227.

4 Z. Zhang, H. Guo, S. Li, S. Gao, X. Wang, M. Li, W. Yan and H. Xu, Cavity-confined Au@Cu2O yolk-shell nanoreactors enable switchable CH4/C2H4 selectivity, *Nat. Commun.*, 2025, **16**, 7559.

5 Y. Zhong, X. Kong, Z. Song, Y. Liu, L. Peng, L. Zhang, X. Luo, J. Zeng and Z. Geng, Adjusting Local CO Confinement in Porous-Shell Ag@Cu Catalysts for Enhancing C–C Coupling toward CO2 Eletroreduction, *Nano Lett.*, 2022, **22**, 2554–2560.

6 S. Chen, Z. Zhu, K. Song, H. Zhang, D. Luo, T. Cao, Y. Zou, C. Liu, L. Gan, D. Zhang, Y. Han and J. Huang, Engineering Cu/Ru heterointerface-shelled nanocavities by the kirkendall effect for highly efficient nitrate electroreduction to ammonia, *J. Am. Chem. Soc.*, 2025, **147**, 36494–36507.

7 T. Hou, X. Li, X. Zhang, R. Cai, Y.-C. Wang, A. Chen, H. Gu, M. Su, S. Li, Q. Li, L. Zhang, S. J. Haigh and J. Zhang, Atomic Au3Cu Palisade Interlayer in Core@Shell Nanostructures for Efficient Kirkendall Effect Mediation, *Nano Lett.*, 2024, **24**, 2719–2726.

8 L. Shen, L. Yu, X. Yu, X. Zhang and X. W. (David) Lou, Self‐Templated Formation of Uniform NiCo2O4 Hollow Spheres with Complex Interior Structures for Lithium‐Ion Batteries and Supercapacitors, *Angew. Chem. Int. Ed.*, 2015, **54**, 1868–1872.

9 H. Wang, E. Feng, Y. Liu and C. Zhang, High-performance hierarchical ultrathin sheet-based CoOOH hollow nanospheres with rich oxygen vacancies for the oxygen evolution reaction, *J. Mater. Chem. A*, 2019, **7**, 7777–7783.

10 J. Wang, L. Zhu, F. Li, T. Yao, T. Liu, Y. Cheng, Z. Yin and H. Wang, Synergizing Phase and Cavity in CoMoOxSy Yolk‐Shell Anodes to Co‐Enhance Capacity and Rate Capability in Sodium Storage, *Small*, 2020, **16**, 2002487.

11 K. Mazloomian, T. R. Dore, H. J. Lancaster, C. A. Howard and T. S. Miller, Synthetic Engineering of Manganese Oxide–Carbon Nanocomposites for Maximized Metal Utilization in Supercapacitors, *Energy Environ. Mater.*, 2025,

e70162.
12 F. Qiao, W. Liu, S. Yu, Q. Zhang, G. Li and H. Chu, Construction of δ-MnO2/Mn2O3 Flower Sphere Composite with Two-Dimensional Hierarchical Nanosheets as Supercapacitor Electrode with Enhanced Performance, *Ceram. Int.*, 2024, **50**, 351–359.
13 N. C. Horti, A. Samage, M. A. Halakarni, S. K. Chavan, S. R. Inamdar, M. D. Kamatagi and S. K. Nataraj, Optical and Electrochemical Properties of Manganese Oxide (Mn3O4) Nanoparticles: Investigating the Influence of Calcination Temperature on Supercapacitor Performance, *Mater. Chem. Phys.*, 2024, **318**, 129276.
14 S. K. Godlaveeti, H. Maseed, A. A. Alothman, A. A. Bin Rasheed, S. Gedi, H. V and R. R. Nagireddy, Boosted Electrochemical Performance of SnO2/Mn3O4-Mn2O3 Composite Supported on Reduced Graphene Oxide for Supercapacitor Applications, *Int. J. Hydrog. Energy*, 2025, **102**, 1399–1410.
15 Z. Lian, X. Mao, Y. Song, K. Yao, R. Zhang, X. Yan and M. Li, The Preparation of High-Performance MoO3 Nanorods for 2.1 V Aqueous Asymmetric Supercapacitor, *Nanomaterials*, 2024, **14**, 2029.
16 K. N. Amba Sankar, L. Kesavan, B. Saha, M. K. Jyolsnaraj, S. Mohan, P. Nandakumar, K. Mohanta and C. Kvarnström, Renewable Synthesis of MoO3 Nanosheets via Low Temperature Phase Transition for Supercapacitor Application, *Sci. Rep.*, 2024, **14**, 20503.
17 W. Wanchan, G. K. Yogesh, R. Yeetsorn, Y. Maiket and P. Koinkar, Synthesis and Characterization of Synergetic Pd/MoO3–rGO Hybrid Material as Efficient Electrode for Supercapacitor Application, *Mater. Chem. Phys.*, 2025, **331**, 130134.
18 S. Ahmed, M. A. Gondal, J. A. Khan, M. A. Almessiere, A. Baykal and A. Ali, Comparative Transition Molybdates (XMoO4 (X = Co, Mn, Ni, and Zn)) for High-Performance Supercapacitors, *Inorg. Chem. Commun.*, 2025, **178**, 114514.
19 A. V. A, A. Singh, N. Tripathy, P. Lakhiwal, M. Iqbal, R. Kumar, M. K. Kashyap, A. D. Sarkar and S. K. Mahapatra, Built-In Electric Field at the Heterojunction of MnMoO4@1T-MoS2 to Enhance the Electrochemical Storage Capacity in All Quasi-Solid-State Supercapacitors, *Adv. Funct. Mater.*, 2025, 2421379.
20 P. Shanmugam, K. Hosomi, R. Rajendran, B. Krishnasamy, M. Kretkowski, W. Inami, Y. Kawata and T. Dheivasigamani, Promising Transition Metal Molybdate (TMM) Single Phase Microstructures for Asymmetric Supercapacitor and Photocatalytic Applications, *Ceram. Int.*, 2024, **50**, 55865–55878.
21 K. Sureshkumar, K. Babu, S. Sakkaraiyan, A. Dinesh, K. Radhakrishnan, L. Gnanasekaran, R. P. Patil, M. Santhamoorthy, M. Iqbal and M. Ayyar, Synthesis of Manganese Molybdate (MnMoO4) Nanorods by Co-Precipitation Method for Supercapacitor Applications, *Semiconductors*, 2024, **58**, 825–833.